第 48 卷 第 20 期/2021 年 10 月/中国激光 研究论文

中国激光

双波长海洋激光雷达探测近岸到大洋水体的叶绿素剖面

李凯鹏[1,2]，贺岩[1*]，侯春鹤[1]，马剑[1]，姜正阳[1]，陈卫标[1**]，陈鹏[3]，刘芳华[1,2]，陈勇强[1,2]，郭守川[1,2]

[1]中国科学院上海光学精密机械研究所空间激光信息传输与探测技术重点实验室，上海 201800；

[2]中国科学院大学材料与光电研究中心，北京 100049；

[3]自然资源部第二海洋研究所卫星海洋环境动力学国家重点实验室，浙江 杭州 310012

摘要 蓝绿激光波段作为海洋主动探测技术中常用的波段，被广泛应用于各种海洋激光雷达设备中。然而由于近岸水体和大洋水体的水质参数不同，不同水体对蓝光和绿光的衰减存在差异。通过反演双波长海洋激光雷达(DWOL)系统中 486 nm 蓝光通道和 532 nm 绿光通道在南海获取的近岸水体和大洋水体探测的波形数据，结果表明：在清洁大洋水域中，486 nm 通道的水体衰减系数明显小于 532 nm 通道，由此说明蓝光更适用于大洋清洁水体探测；在近岸水域中，由于水质变差，486 nm 通道和 532 nm 通道的衰减系数差异减小，同时考虑到 532 nm 激光的稳定性和低成本，可知绿光更适用于近岸水体探测。另外，为了分析南海水域次表面层叶绿素散射层(CSL)从近岸水体到大洋水体的分布变化，基于 486 nm 通道数据，反演了从清洁大洋水域到近岸水域近 120 km 连续条带的机载数据。反演结果表明：在大洋水体中，CSL 深度稳定分布在水下 60 m 左右；在临近近岸时，由于水深变浅，CSL 深度分布开始快速上升；在近岸水体中，CSL 深度上升到水下 40 m，甚至到 20 m 左右。分析船测实验数据与机载反演数据的相关关系，可知机载反演结果和船测结果具有良好的一致性。

关键词 遥感；双波长激光雷达；叶绿素散射层；激光雷达反演；Klett 方法

中图分类号 O439 **文献标志码** A **doi**：10.3788/CJL202148.2010002

1 引 言

海洋水体中次表面层叶绿素分布作为一项海洋遥感中的重要指标，在全球海洋碳循环过程研究中扮演着重要的角色[1]。获取海洋水体中的叶绿素分布情况的技术主要可以采用被动水色遥感技术和主动探测技术。传统被动水色遥感的方法经过过去几十年的发展，深刻改变了人们对海洋中叶绿素悬浮层分布的认知。然而，作为一项被动遥感技术，水色遥感方法仅能获取所测海域中上层水体参数的积分信息，不能提供具备距离分辨的水体剖面信息，因而主要用于大尺度范围浮游生物总量的表征[2]。在自然水域中，由于营养盐梯度和自然光照条件等因素的综合作用，水体中次表面层形成叶绿素分布的极大值悬浮层，即叶绿素散射层[3](CSL)。基于此，主动探测技术，例如海洋激光雷达技术可以很好地弥补被动光学遥感的不足，能够提供水体中具备距离分辨的叶绿素悬浮层的垂直剖面信息。特别是近些年来，主动海洋激光雷达探测技术在海洋次表面层浮游生物的研究取得了广泛的进展[4-7]。

在海洋光学探测中，海水对蓝绿波段的入射波段具有较小的衰减系数，故蓝绿波段称之为海洋透射窗口[8-10]，常被用于海洋激光雷达系统中。一方面，在近岸水体中，由于水体中悬浮颗粒物和有色溶解有机物(CDOM)的衰减和吸收，蓝光波段相比绿光波段优势不大，同时蓝光波段需要使用光学参量放大(OPO)技术产生，成本较高。另一方面，绿光波段光源，例如 532 nm 光源，成本较低，性能稳定，

收稿日期：2021-03-01；**修回日期**：2021-03-16；**录用日期**：2021-03-29

基金项目：自然资源部第二海洋研究所卫星海洋环境动力学国家重点实验室重点研发项目(2016YFC1400902)、青岛海洋科学与技术国家实验室区域海洋动力学与数值模拟功能实验室开放基金项目(2018SDKJ0102-7)

通信作者：*heyan@siom.ac.cn； **wbchen@siom.ac.cn

并且可以提供较高能量的窄脉宽脉冲光，因而532 nm 光源被广泛用于常见的海洋雷达系统中，包括船载、机载和星载海洋激光雷达系统[11-13]。

然而在较清洁的大洋水体探测中，随着 CDOM 含量的减少，水体对蓝光波段的衰减减小，因而最佳的探测波段向蓝光波段偏移。为了分析蓝绿激光波段在近岸水体和大洋水体中的探测差异，中国科学院上海光学精密机械研究所研制了一套搭载 486 nm 蓝光波段和 532 nm 绿光波段的双波长激光雷达系统(DWOL)，利用新搭载的蓝光波段实现了清洁大洋水体和近岸水体的兼容探测[14]，同时该系统也可用于研究不同波段激光光束的联合探测[15-17]。基于该系统进行了机载实验，并根据实验结果进行反演，得到了南海水域中近岸水体和大洋水体不同水质下的水体衰减系数的剖面分布。

为了反映南海水域中次表面层 CSL 从近岸水域到大洋水域的分布变化，反演了从近岸水域到大洋水域约 120 km 连续条带的飞行数据，讨论了南海水域中叶绿素悬浮层垂直剖面分布随水深的变化情况。

2 系统设计

图 1 展示了 DWOL 系统的设计原理。该系统主要由三个部分组成：激光发射子系统，系统接收子系统，采集和存储系统。激光发射系统主要包含双波长激光器和发射转折镜(TM)；接收系统主要包含接收主望远镜、双胶合准直镜(CL)、分光镜(LDM)以及滤光片等。在每个通道的终端均配有一个光电倍增管(PMT)探测器，用于探测回波信号。探测器的输出信号由信号采集和接收系统中的信号采集卡接收，并存储于固态硬盘(SSD)中。本系统还配备了上位机系统，用于控制指令的输入和回波信号的实时预览。系统的设计指标如表 1 所示。

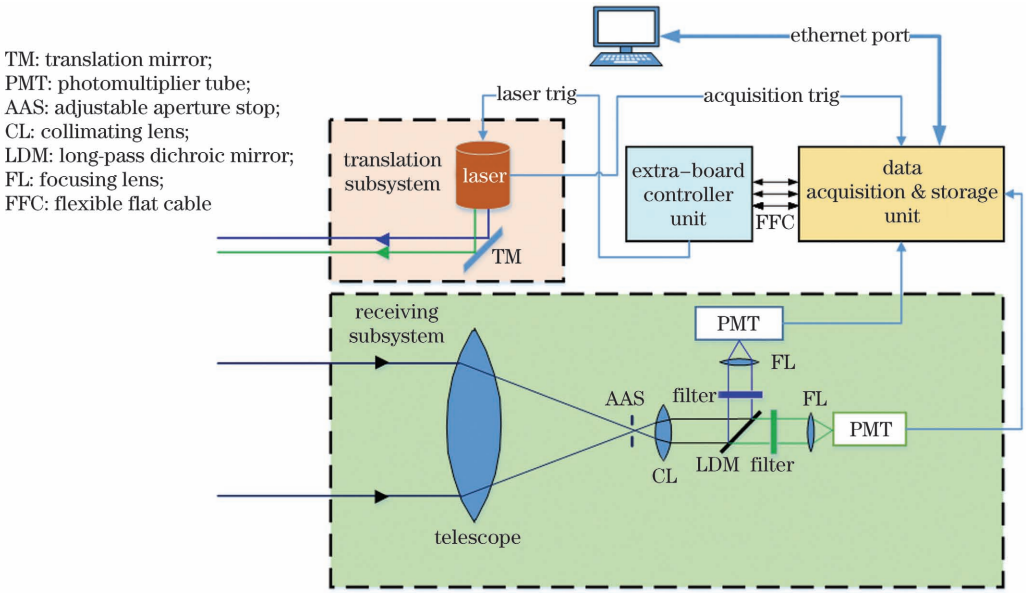

图 1 双波长海洋激光雷达系统结构示意图

Fig. 1 Schematic diagram of the DWOL system

表 1 双波长海洋激光雷达系统设计参数

Table 1 Parameters designed for the DWOL system

Apparatus	Parameter	Value
Transmitter	Wavelength /nm	486 & 532
	Pulse energy /mJ	2.7 at 486 nm & 5.4 at 532 nm
	Repetition rate of laser /Hz	100
	Pulse width /ns	8.7 at 532 nm & 4 at 486 nm
	Beam divergence /mrad	4.7 at 486 nm & 2.4 at 532 nm
Receiver	Diameter of telescope /mm	200
	Maximal field of view /mrad	20
	Optical efficiency	0.6
	Efficiency of PMT	0.10
	Time sampling resolution /ns	10
	Height of plane /m	2000–3000
	Speed of plane /(km·h^{-1})	200

2.1 发射子系统

发射子系统主要包含双波长激光器和发射转折镜。双波长激光器的工作原理图和激光器内部结构如图 2 所示[18]。

双波长激光器可以同时发射 486 nm 和 532 nm 的激光束，其中 532 nm 激光可以由 1064 nm 激光通过三硼酸锂(LBO)晶体倍频得到，486 nm 激光束可通过偏硼酸钡(BBO)晶体经过光学参量振荡器(OPO)产生，486 nm 和 532 nm 激光器的能量分别为 2.7 mJ 和 5.4 mJ。

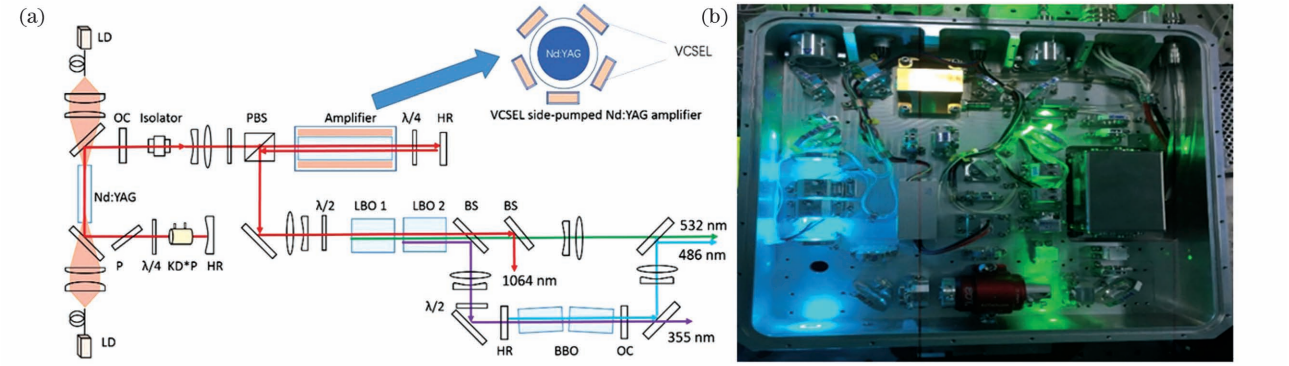

LD: laser diode; OC: output coupler; PBS: polarization beam splitter; HR: highly reflective plane-concave mirror; VCSEL: vertical cavity surface-emitting laser; LBO: lithium triborate crystal; BBO: type I beta-barium borate crystal; LDM: long-pass dichroic mirror

图 2 486 nm & 532 nm 激光器原理图和结构图[18]。(a)激光器原理图；(b)激光器内部结构图

Fig. 2 Schematic diagram of 486 nm & 532 nm lasers[18]. (a) Schematic diagram of the laser; (b) internal structure of the lasers

2.2 接收子系统

接收子系统主要由接收望远镜和后续的分光光路组成，当 532 nm 和 486 nm 的信号回波光同时到达系统接收主望远镜的前端时，信号经接收主望远镜会聚到可变光阑处，可变光阑可以根据信号回波的情况进行调节。在本次实验中，可变光阑的光阑尺寸设置为 20 mrad。信号光经过可变光阑后将由双胶合准直镜准直成平行光束，平行光束经过分光镜后，分成两束信号光，即 486 nm 信号光和 532 nm 信号光，这两束信号光分别进入对应的 486 nm 通道和 532 nm 通道中。在每个接收通道终端，均配备有 PMT 探测器，回波光信号经 PMT 探测器转化为相应的电信号并被模数(AD)采集卡采集获取，最终存储于固态硬盘(SSD)中。AD 采集卡的通道精度为 10 bit，模拟信号和数字信号之间的转换关系为

$$V_a = \frac{2.0}{1024} V_d, \tag{1}$$

式中，V_a 和 V_d 分别为模拟信号响应和数字信号。AD 采集卡的采样频率为 1 GHz，该双波长激光雷达系统的时间分辨率为 1 ns。

3 实验结果分析与讨论

3.1 机载双波长激光雷达飞行实验数据

为了分析南海水域次表面层 CSL 从近岸水体到大洋水体的分布变化，双波长海洋激光雷达系统搭载飞行平台于 2019 年 6 月 1 日在中国南海海域中(东经 109.8°～110.8°，北纬 17.4°～17.8°)进行了飞行实验。针对从近岸水域到大洋水域连续 120 km 的飞行条带 Swath-B 至 Swath-A 中 4 个点(S1，S2，S3，S4)的 486 nm 通道反演数据进行分析，其中 S1 点位于近岸水域，S4 点位于大洋水域。文中的水深数据源于文献[19]。在飞行实验中，探测器设置为高增益模式，在该种模式下，探测器可以同时接收来自上层水体的连续回波信号和来自深层水体的离散单光子信号。图 3 展示了 DWOL 系统获取的来自大洋水体中 S4 点和近岸水体 S1 点的单帧波形数据。

由图 3 的结果可以看出，在清洁大洋水体中，486 nm 相对于 532 nm 的衰减明显偏小，能够探测到更深的水域。在近岸水体中，由于近岸水体的水质变差，486 nm 相对于 532 nm 的探测优势开始减弱。

由于实验是在晚上进行的，环境背景光信号较弱，故来自深层水体的离散单光子信号可以被提取出来。回波光子数和 AD 采集卡采集到的回波信号之间的关系可表示为

$$N = \frac{V_d - V_{baseline}}{V_{unit}}, \tag{2}$$

式中：V_d 为 AD 采集卡采集到的数字信号；$V_{baseline}$ 为 AD 采集卡采集到的探测器系统的本底基线值；V_{unit} 为单光子响应幅值，可以在探测器厂商提供的

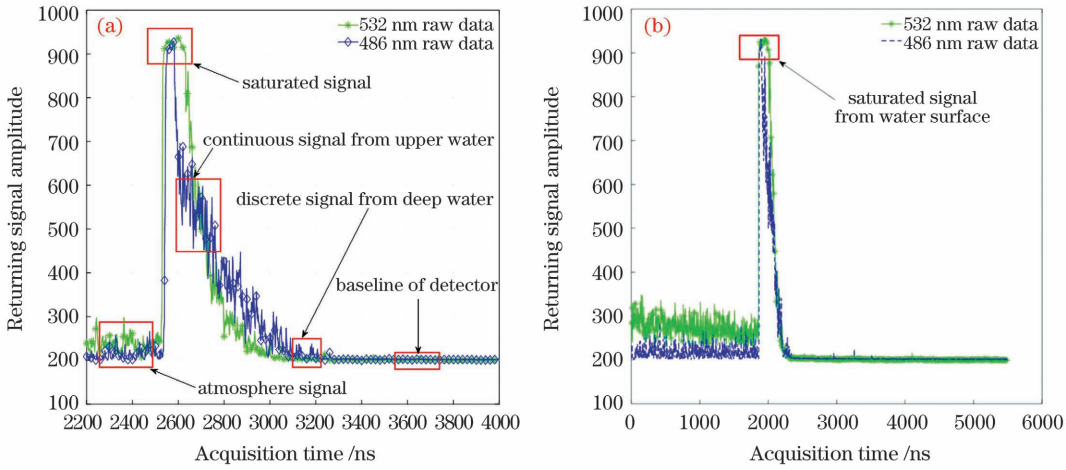

图 3 机载实验结果。(a)大洋水体单帧数据结果;(b)近岸水体单帧数据结果

Fig. 3 Airborne results. (a) Result for one frame of data from oceanic water at S4; (b) result for one frame of data from coastal water at S1

数据手册中查找获得。本次实验中,532 nm 和 486 nm 的单光子响应幅值分别为 8 和 10。探测器本底基线 V_{baseline} 的确定方法来自文献[14]。

在 DWOL 系统中,PMT 探测器在高增益模式下,接收到来自上层水体的强脉冲回波信号后,产生一系列后脉冲(APC)噪声。该 APC 信号将影响对深层水体信号的反演结果[20-23]。APC 噪声的滤除方法参考文献[14]。同时,考虑到飞机航速为 50 m/s,激光器重复频率为 100 Hz,为了增大系统的探测动态范围,将 5 s 内的数据进行累加,经过处理后 DWOL 系统在清洁大洋水域和近岸水域中获取的水体剖面回波信号分别如图 4(a)和图 4(b)所示。

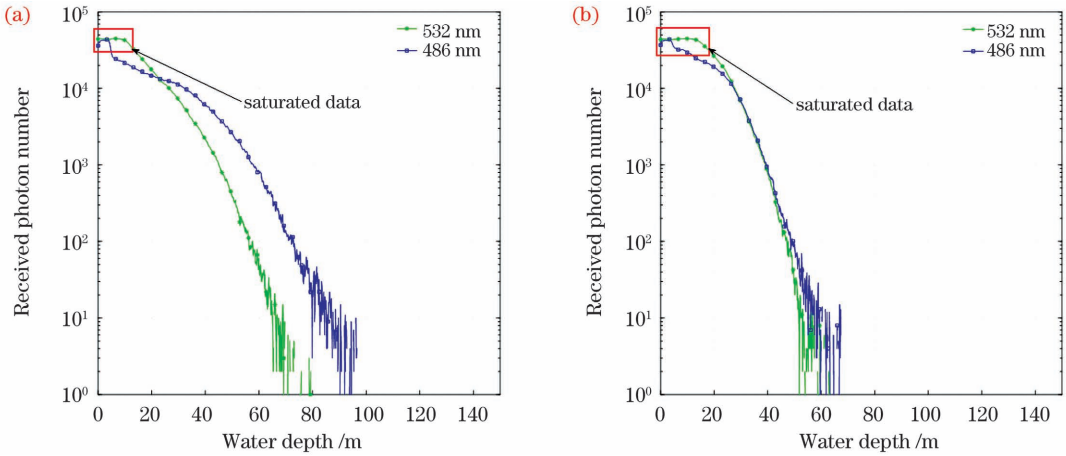

图 4 500 帧数据的累加结果。(a)大洋水域 S4 点的结果;(b)近岸水域 S1 点的结果

Fig. 4 Accumulation for 500-frame data. (a) From oceanic water at S4; (b) from coastal water at S1

由图 4 可知,486 nm 通道在清洁大洋水体中获取的水体剖面深度将近 100 m,相较于 532 nm 通道,探测深度增加了 25%。而在近岸水体中,由于近岸水体的水质变差,486 nm 通道相较于 532 nm 通道的探测优势减弱。

为了反演南海所测水域的水质参数,同时进一步比较 486 nm 通道和 532 nm 通道的探测差异,需要对机载数据进行进一步反演。另外,为了避免深层水体反演结果受上层水体强回波信号所导致的 APC 噪声以及上层水体饱和信号的影响,在本次机载数据反演处理中主要采用水下 6 m 至水下 80 m 之间的回波数据进行反演处理。

3.2 机载实验结果反演

水体信号的激光雷达方程可以表示为[24]

$$P(z)=K\frac{\beta(\pi,z)}{(nH+z)^2}\exp\left[-2\int_0^z\alpha(z')\mathrm{d}z'\right],\tag{3}$$

式中,$P(z)$为 z 处的回波信号,K 为激光雷达常数,$\beta(\pi,z)$为 π 方向的体散射函数,n 为水体折射率,H 为航高,$\alpha(z)$为激光雷达消光系数。为了反演激光雷达消光系数,采用 Klett 方法进行反演,Klett 方法由表示为[25]

$$\alpha(z)=\frac{\exp\left[\frac{S(z)-S_m}{k}\right]}{\frac{1}{\alpha_m}+\frac{2}{k}\int_z^{z_m}\exp\left[\frac{S(z)-S_m}{k}\right]\mathrm{d}z},\quad(4)$$

式中：S_m 为回波信号的边界值；α_m 为激光雷达消光系数的边界值，可以由斜率法得到[26]；k 为 $\beta(\pi,z)$ 和 $\alpha(z)$ 之间的系数，此处取为 1；$S(z)$ 为激光雷达系统所接收到的经过距离校正的回波信号的对数形式，即

$$S(z)=\ln[P(z)\times(nH+z)^2]。\quad(5)$$

利用 (4) 式和(5) 式反演了 486 nm 和 532 nm 通道的激光雷达消光系数在 S4 点和 S1 点的分布，如图 5 所示。

由图 5 的结果可知：在大洋水体中 486 nm 和 532 nm 通道的水体衰减系数有明显差异，486 nm 通道的衰减系数比 532 nm 通道的衰减系数明显小一些，因而 486 nm 通道对于大洋水体的探测有明显优势；532 nm 通道所探测到的数据中 60 m 以下的数据质量较差，这表明 532 nm 的数据在 60 m 以下时数据反演可信度降低，因而大洋水体的反演中 486 nm 通道的数据更可靠。然而，在近岸水体中，由于水质变差，532 nm 和 486 nm 的衰减系数差异变小，这表明 486 nm 在近岸水体的探测相较于 532 nm 的探测优势消失。

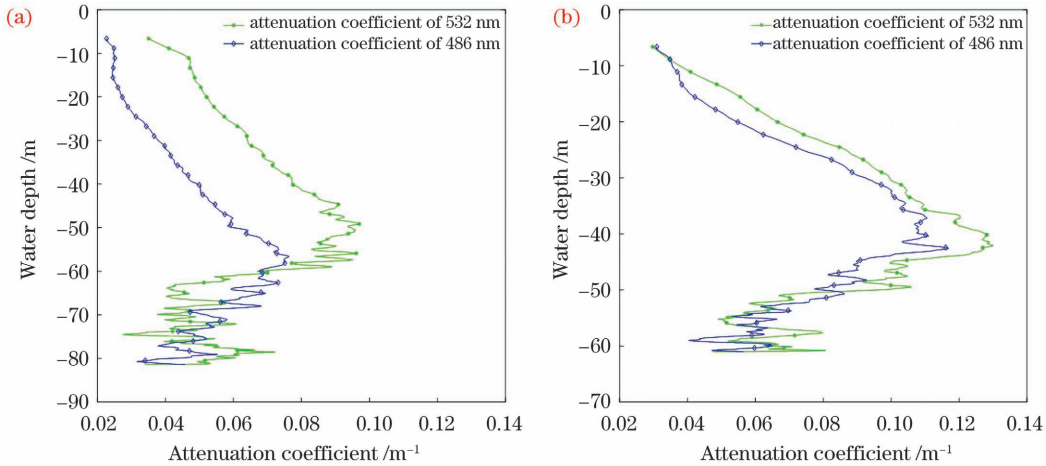

图 5 486 nm 通道和 532 nm 通道在 S4 和 S1 点处的水体衰减系数。(a)S4 点处；(b)S1 点处

Fig. 5 Attenuation coefficients of water for 486 nm channel and 532 nm channel at S4 and S1. (a) At S4; (b) at S1

3.3 船载实验结果对比

为了验证机载实验的数据，在测区范围内进行了同步的船载实验。近岸水域的实测点以 E、F 以及 D1 标号，大洋水域的实测点以 A、B、C、D2 以及 G 标号。利用船载的水质剖面测量仪(RBR XR-420，RBR Ltd.，Canada)设备测量了从大洋深层水体到近岸浅层水体中的叶绿素分布情况，如图 6 和图 7 所示。

由船测数据可以看出，在大洋水体中叶绿素悬浮层分布在水下 50～60 m，并且在深水区叶绿素悬浮层在水体中的质量浓度为 1 $\mu g\cdot L^{-1}$ 左右。在近岸水体中，由于水深变浅，叶绿素悬浮层开始快速上升，在近岸处叶绿素悬浮层分布于 20～40 m 之间，叶绿素峰值浓度上升到 1.5 $\mu g\cdot L^{-1}$。

考虑到在大洋水体中叶绿素浓度极大值主要分布在水下 60 m 左右，结合图 4 和图 5 的结果可知，532 nm 的数据在 60 m 以下的数据可靠性减弱。为了得到稳健的叶绿素反演结果，并全面反映南海水域特别是大洋水域到近岸水域中叶绿素分布的连续变化特征，在叶绿素反演中，主要利用 486 nm 通道数据进行反演。

根据文献[27]可知，漫射衰减系数 K_d 与叶绿素浓度 $\rho_{\text{Chl-a}}$ 之间的生物光学模型关系为

$$K_d(\lambda)=K_w(\lambda)+K_{bio}(\lambda),\quad(6)$$

$$K_{bio}(\lambda)=\chi(\lambda)\times C^{e(\lambda)},\quad(7)$$

式中：$K_w(\lambda)$ 为 λ 波段对应的纯水的漫射衰减系数；$K_{bio}(\lambda)$ 为与叶绿素浓度相关的颗粒物漫射衰减系数；$\chi(\lambda)$ 和 $e(\lambda)$ 为模型的缩比因子，可以由文献[28]得到。由于激光雷达系统在水面的视场角较大，激光雷达消光系数可以使用漫射衰减系数 K_d 表示[29]。基于 (3)～(7) 式，反演了机载航线选取点 S1，S2，S3，S4 的 486 nm 通道数据。结果如图 8 所示。

图 8 的反演结果表明，近岸水域 S1 点到大洋水域 S4 点的叶绿素悬浮层的深度逐渐变深。为了验证 486 nm 通道数据在大洋水域和近岸水域反演结果的有效性，基于船载实测站点 F6，D1，C1，B3 点的实测数据与机载航线选取点 S1，S2，S3，S4 点的 486 nm 通道数据的反演结果进行相关性分析。

分析在对应深度下，船载实测结果和486 nm

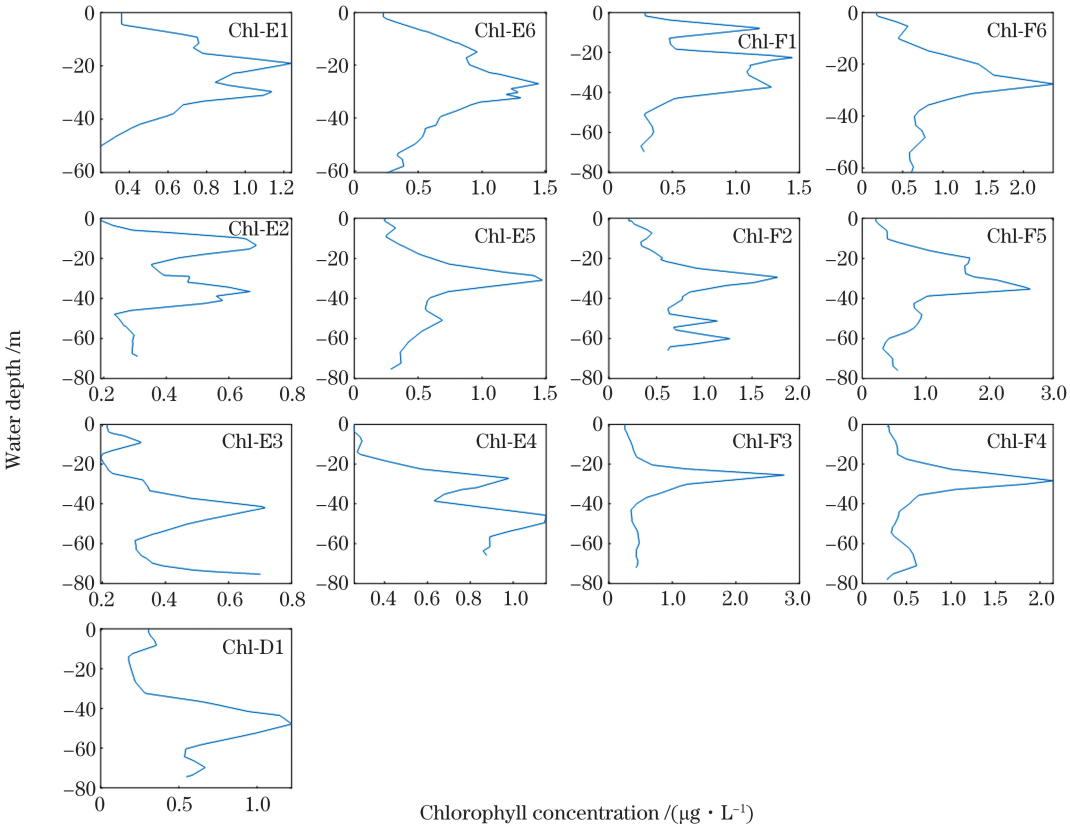

图 6 船测实验获取的近岸水体中叶绿素浓度剖线

Fig. 6 Profiles of chlorophyll concentration in coastal water obtained in the *in-situ* shipborne experiment

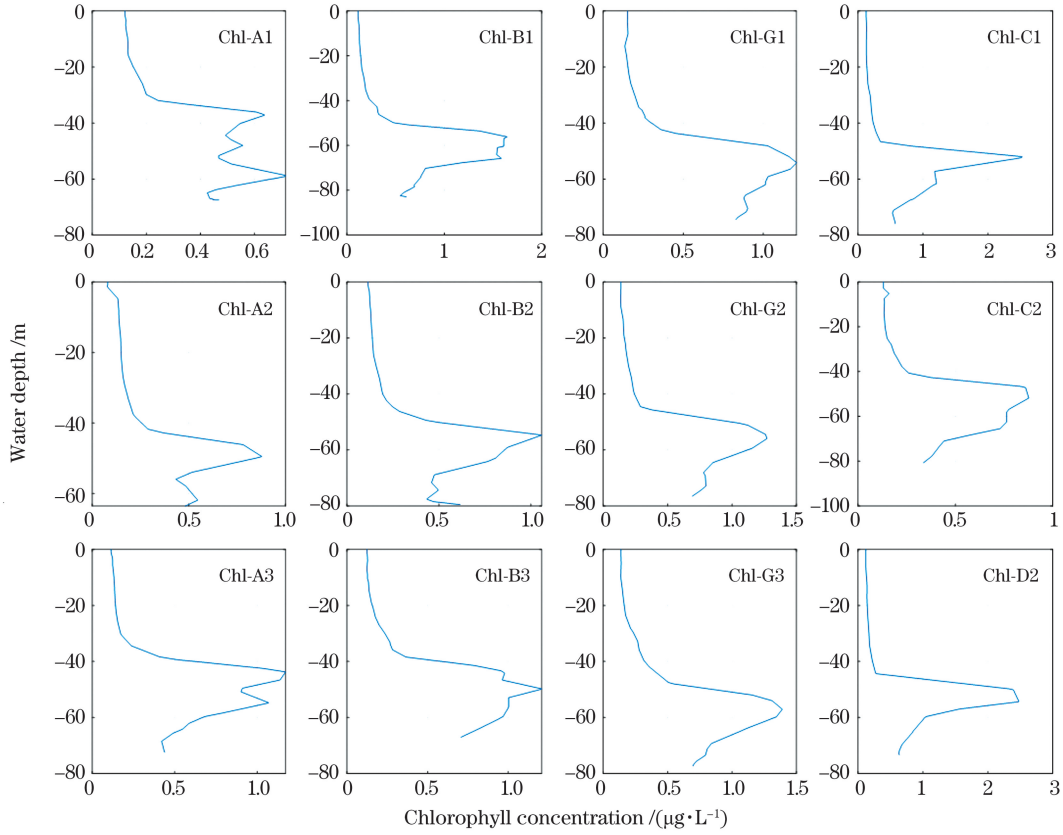

图 7 船测实验获取的大洋水体叶绿素浓度剖线

Fig. 7 Profiles of chlorophyll concentration in oceanic water obtained in the *in-situ* shipborne experiment

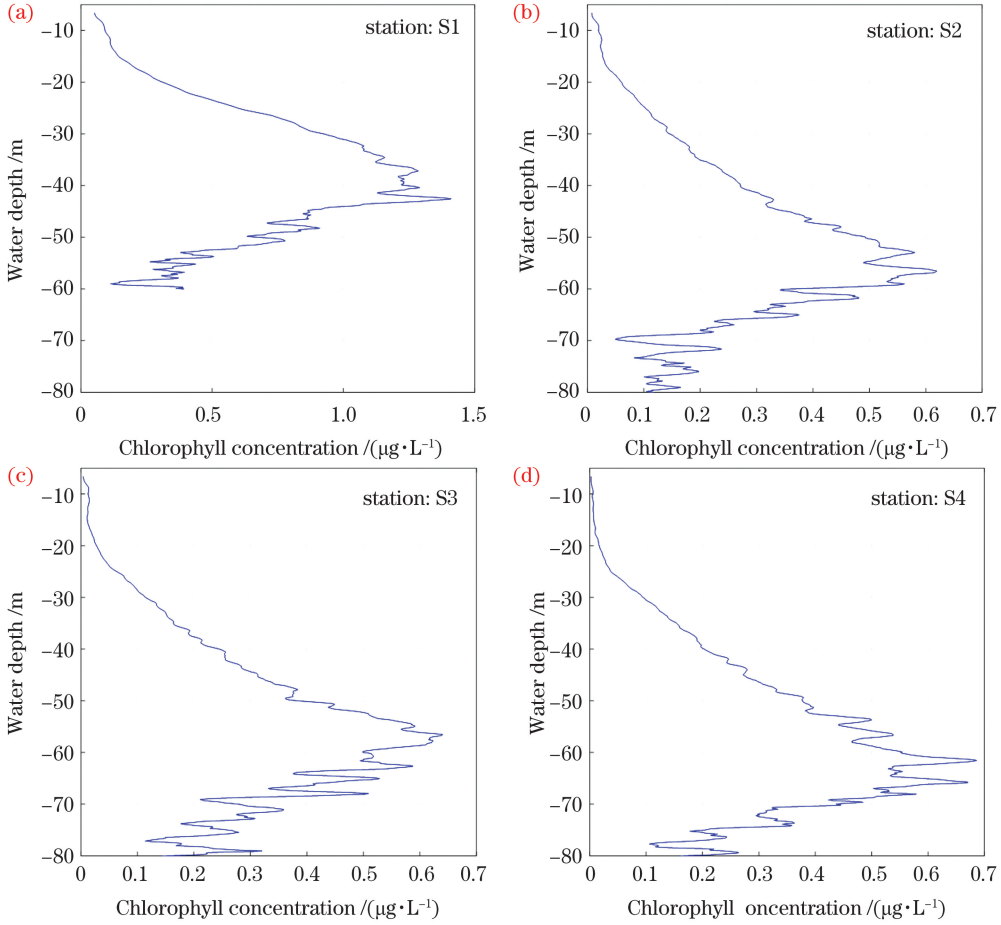

图 8 486 nm 通道数据反演得到的叶绿素浓度。(a)S1 点处;(b)S2 点处;(c)S3 点处;(d)S4 点处

Fig. 8 Chlorophyll concentration inversed with 486 nm data. (a) At S1; (b) at S2; (c) at S3; (d) at S4

通道数据反演结果的一致性,结果如图 9 所示。由图 9 的结果可知,在对应深度下,船载实测叶绿素浓度数据和机载反演数据的相关性决定因子 $R^2>0.8$,这表明 486 nm 通道的机载反演结果和船载实测数据具有良好的一致性,证明了基于 DWOL 系统 486 nm 波段反演南海水域水体中 CSL 分布的有效性。

为了反映从大洋水体到近岸水体中水质剖面参数和 CSL 分布的连续变化,选取从大洋水体到近岸水体连续 120 km 的飞行条带 Swath-AB,反演 Swath-AB 条带中的 486 nm 通道数据。飞行条带的反演结果如图 10 所示。

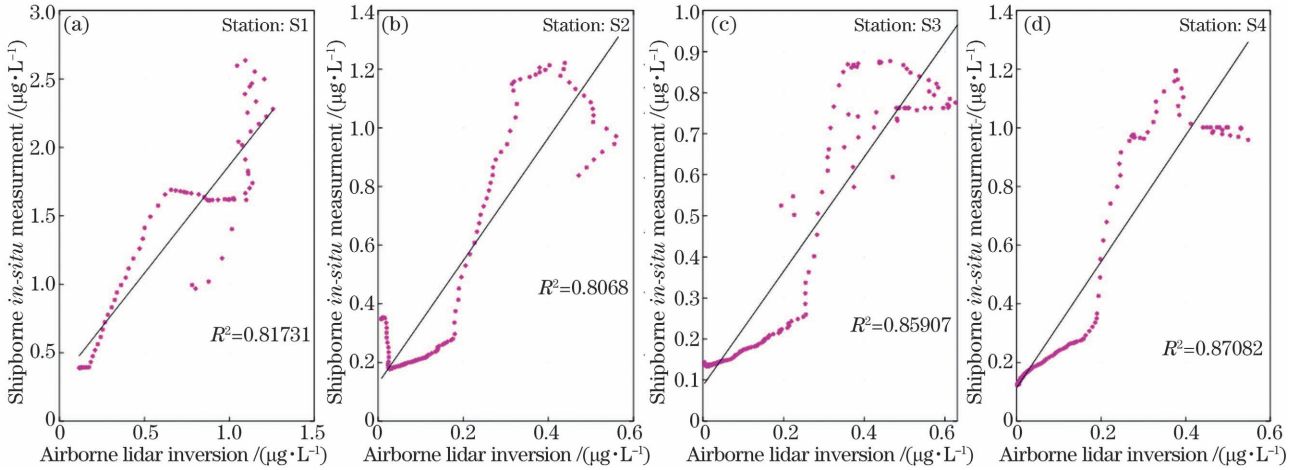

图 9 对应深度下机载数据反演结果和船载实测结果的相关性分析。(a)S1 点处;(b)S2 点处;(c)S3 点处;(d)S4 点处

Fig. 9 Correlation analysis between the airborne data inversion results and shipborne measurement results at corresponding depth. (a) At S1; (b) at S2; (c) at S3; (d) at S4

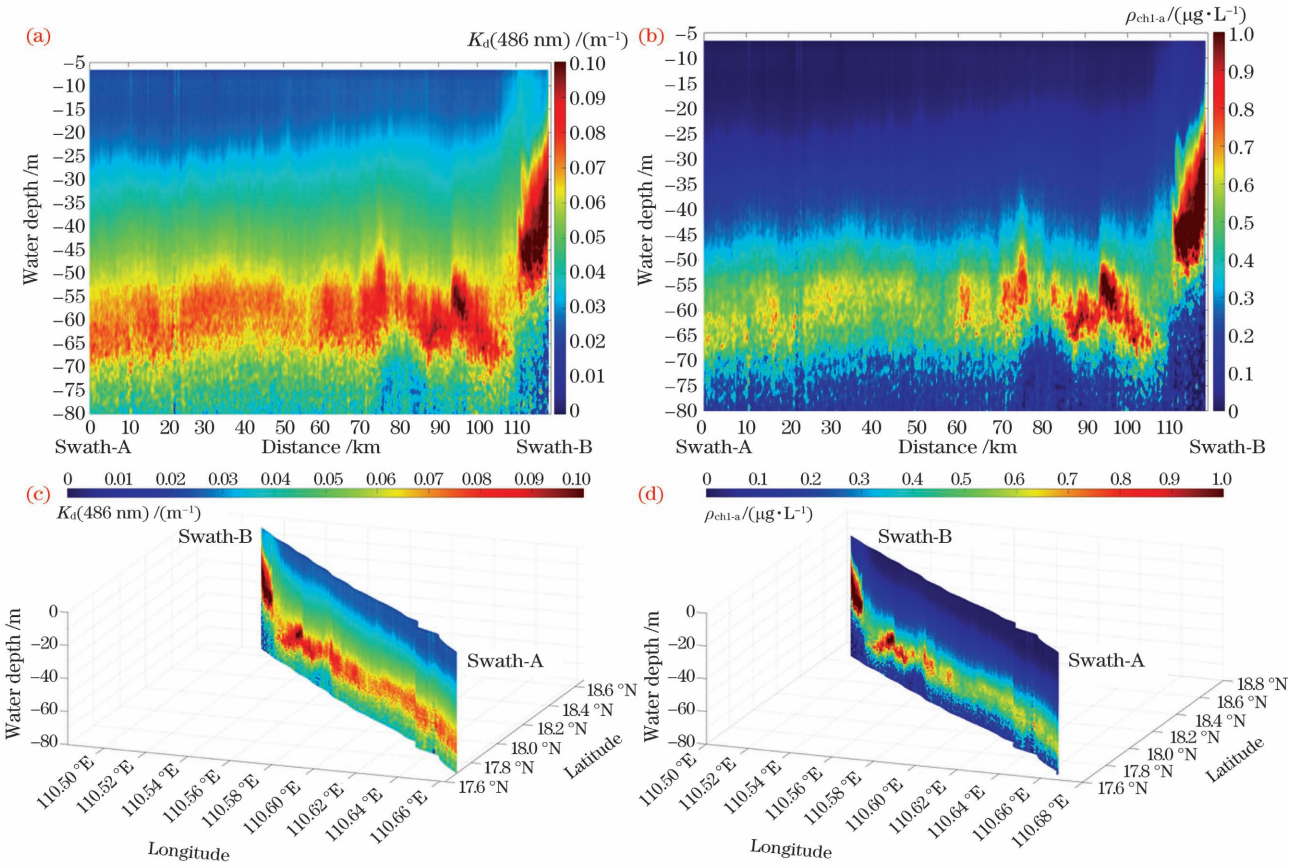

图 10 水体衰减系数剖面分布与叶绿素悬浮层剖面分布。(a)(c) 水体衰减系数剖面分布;(b)(d) 叶绿素悬浮层剖面分布

Fig. 10 Distribution of attenuation coefficients profiles and the corresponding distribution of CSL profiles. (a)(c) Distribution of attenuation coefficients profiles; (b)(d) corresponding distribution of CSL profiles

由反演结果可知,在清洁大洋水体中,CSL 悬浮层主要分布于水下 60 m 左右,反演结果在大洋水体岸到近岸的很长一段距离内保持稳定。在近岸水体中,由于水深变浅,CSL 开始快速上浮,其深度分布于水下 20 m 到水下 40 m 之间。

4 结 论

基于双波长海洋激光雷达在南海水域的机载实验数据,反演了大洋水域和近岸水域的水质参数。反演结果表明:在清洁大洋水体中,486 nm 蓝光的衰减系数相比 532 nm 绿光明显较小,表明蓝光更适用于清洁大洋水体剖面的探测;在近岸水体中,486 nm 和 532 nm 的水体衰减系数差异减小,表明蓝光在近岸水体剖面的探测优势减弱。考虑到 486 nm 激光需要利用 OPO 技术产生,设备运行条件较为苛刻,单脉冲能量相较于 532 nm 较低,故 532 nm 绿光更适用于近岸水体剖面的探测。

为了反映南海水域次表面层 CSL 的分布特征,基于 486 nm 通道数据反演了从大洋水体到近岸水体约 120 km 连续条带的机载数据。反演结果表明,南海水域中 CSL 主要分布于水下 60 m 左右的水深范围内,且从大洋水体到近岸水体中 CSL 的深度变化不大。在近岸水域中,由于水深变浅,CSL 开始快速上浮,其分布深度上升至水下 40 m,甚至到 20 m。船载实测数据和机载反演数据在对应深度下的相关性决定因子 $R^2>0.8$,表明机载数据反演结果和船载实测结果具有良好的一致性,证明了 486 nm 激光用于南海水域水体叶绿素悬浮层剖面探测的有效性。接下来的工作,一方面将进一步研究双波长海洋激光雷达系统的误差来源,提高探测数据的可靠性,另一方面将研究双波长激光雷达在中国更多海域中的应用效果,评估双波长海洋激光雷达系统在海洋水体剖面探测中的适用性。

参 考 文 献

[1] Behrenfeld M J, Worthington K, Sherrell R M, et al. Controls on tropical Pacific Ocean productivity revealed through nutrient stress diagnostics [J]. Nature, 2006, 442(7106): 1025-1028.

[2] Ryther J H, Yentsch C S. The estimation of phytoplankton production in the ocean from

chlorophyll and light data [J]. Limnology and oceanography, 1957, 2(3): 281-286.

[3] Ryan J P, McManus M A, Sullivan J M. Interacting physical, chemical and biological forcing of phytoplankton thin-layer variability in Monterey Bay, California[J]. Continental Shelf Research, 2010, 30(1): 7-16.

[4] Churnside J H, Marchbanks R D, Vagle S, et al. Stratification, plankton layers, and mixing measured by airborne lidar in the Chukchi and Beaufort seas [J]. Deep Sea Research Part II: Topical Studies in Oceanography, 2020, 177: 104742.

[5] Moore T S, Churnside J H, Sullivan J M, et al. Vertical distributions of blooming cyanobacteria populations in a freshwater lake from LIDAR observations[J]. Remote Sensing of Environment, 2019, 225: 347-367.

[6] Liu H, Chen P, Mao Z H, et al. Subsurface plankton layers observed from airborne lidar in Sanya Bay, South China Sea[J]. Optics Express, 2018, 26(22): 29134-29147.

[7] Schulien J A, Behrenfeld M J, Hair J W, et al. Vertically resolved phytoplankton carbon and net primary production from a high spectral resolution lidar[J]. Optics Express, 2017, 25(12): 13577-13587.

[8] Sogandares F M, Fry E S. Absorption spectrum (340–640 nm) of pure water. Ⅰ. Photothermal measurements[J]. Applied Optics, 1997, 36(33): 8699-8709.

[9] Pope R M, Fry E S. Absorption spectrum (380–700 nm) of pure water. Ⅱ. Integrating cavity measurements[J]. Applied optics, 1997, 36(33): 8710-8723.

[10] Smith R C, Baker K S. Optical properties of the clearest natural waters (200-800 nm)[J]. Applied Optics, 1981, 20(2): 177-184.

[11] Morel A. Light and marine photosynthesis: a spectral model with geochemical and climatological implications[J]. Progress in Oceanography, 1991, 26(3): 263-306.

[12] Roesler C S, Perry M J, Carder K L. Modeling in situ phytoplankton absorption from total absorption spectra in productive inland marine waters [J]. Limnology and Oceanography, 1989, 34(8): 1510-1523.

[13] Bricaud A, Morel A, Prieur L. Absorption by dissolved organic matter of the sea (yellow substance) in the UV and visible domains [J]. Limnology and oceanography, 1981, 26(1): 43-53.

[14] Li K P, He Y, Ma J, et al. A dual-wavelength ocean lidar for vertical profiling of oceanic backscatter and attenuation[J]. Remote Sensing, 2020, 12(17): 2844.

[15] Gray D J, Anderson J, Nelson J, et al. Using a multiwavelength LiDAR for improved remote sensing of natural waters[J]. Applied Optics, 2015, 54(31): F232-F242.

[16] Burton S P, Ferrare R A, Hostetler C A, et al. Aerosol classification using airborne high spectral resolution lidar measurements: methodology and examples [J]. Atmospheric Measurement Techniques, 2012, 5(1): 73-98.

[17] Sasano Y, Browell E V. Light scattering characteristics of various aerosol types derived from multiple wavelength lidar observations[J]. Applied Optics, 1989, 28(9): 1670-1679.

[18] Ma J, Lu T T, He Y, et al. Compact dual-wavelength blue-green laser for airborne ocean detection lidar[J]. Applied Optics, 2020, 59(10): C87-C91.

[19] Amante C, Eakins B W. ETOPO1 arc-minute global relief model: procedures, data sources and analysis [EB/OL]. (2021-01-12)[2021-02-25]. http://www.ngdc.noaa.gov/mgg/global/global.html.

[20] Acharya Y B, Sharma S, Chandra H. Signal induced noise in PMT detection of lidar signals [J]. Measurement, 2004, 35(3): 269-276.

[21] Zhao Y. Signal-induced fluorescence in photomultipliers in differential absorption lidar systems [J]. Applied Optics, 1999, 38(21): 4639-4648.

[22] Concannon B M, Contarino V M, Allocca D M, et al. Characterization of signal-induced artifacts in photomultiplier tubes for underwater lidar applications [J]. Proceedings of SPIE, 1999, 3761: 167-173.

[23] Donovan D P, Whiteway J A, Carswell A I. Correction for nonlinear photon-counting effects in lidar systems[J]. Applied Optics, 1993, 32(33): 6742-6753.

[24] Churnside J H, Marchbanks R D. Inversion of oceanographic profiling lidars by a perturbation to a linear regression[J]. Applied Optics, 2017, 56(18): 5228-5233.

[25] Klett J D. Stable analytical inversion solution for processing lidar returns[J]. Applied Optics, 1981, 20(2): 211-220.

[26] Chen P, Pan D L. Ocean optical profiling in South China sea using airborne LiDAR [J]. Remote Sensing, 2019, 11(15): 1826.

[27] Gordon H R, Morel A Y. Remote assessment of ocean color for interpretation of satellite visible imagery: a review [M]. Washington, D. C.:

American Geophysical Union, 1983.

[28] Morel A, Maritorena S. Bio-optical properties of oceanic waters: a reappraisal [J]. Journal of Geophysical Research: Oceans, 2001, 106 (C4): 7163-7180.

[29] Gordon H R. Interpretation of airborne oceanic lidar: effects of multiple scattering [J]. Applied Optics, 1982, 21(16): 2996-3001.

Detection of Chlorophyll Profiles from Coastal to Oceanic Water by Dual-Wavelength Ocean Lidar

Li Kaipeng[1,2], He Yan[1*], Hou Chunhe[1], Ma Jian[1], Jiang Zhengyang[1], Chen Weibiao[1**], Chen Peng[3], Liu Fanghua[1,2], Chen Yongqiang[1,2], Guo Shouchuan[1,2]

[1] *Key Laboratory of Space Laser Communication and Detection Technology, Shanghai Institute of Optics and Fine Mechanics, Chinese Academy of Sciences, Shanghai* 201800, *China*;

[2] *Center of Materials Science and Optoelectronics Engineering, University of Chinese Academy of Sciences, Beijing* 100049, *China*;

[3] *State Key Laboratory of Satellite Ocean Environment Dynamics, Second Institute of Oceanography, Ministry of Natural Resources, Hangzhou, Zhejiang* 310012, *China*

Abstract

Objective Marine phytoplankton is crucial to the marine ecosystem due to their important roles in the global primary carbon cycle. They can also be used as an evaluation criterion of water property because of their correction to the watercolor remote sensing parameters. Two detection schemes are often used to obtain the distribution of subsurface phytoplankton, including passive remote sensing technology, such as ocean color remote sensing technology, and activity detection technology, for instance, ocean lidar. The ocean color remote sensing is a practical approach to detecting chlorophyll-a (Chl-a) which is a proxy of phytoplankton. However, as a passive remote sensing scheme, the ocean color remote sensing system can only obtain the integral information of upper waters. The vertical distribution of subsurface phytoplankton in the ocean is significantly important for ocean remote sensing study. To obtain the depth-resolved profiles of Chl-a concentration, it is necessary to use the active detection system, such as the ocean lidar system. The conventional ocean lidar systems are often equipped with 532 nm lasers; the 532 nm laser is robust and cost effective and can penetrate ocean water with high-energy pulses. However, a blue laser penetrates and detects clean ocean waters better than a green laser with the same pulse energy. This study presents a novel dual-wavelength ocean lidar (DWOL) system equipped with a dual-wavelength laser, which can emit 532 and 486 nm lasers simultaneously. An airborne experiment and a shipborne *in-situ* experiment were conducted in the South China Sea to validate the performance of DWOL; the airborne data has been processed to inverse the vertical Chl-a concentration. We hope that our novel DWOL system can be useful in researching the vertical distribution of the subsurface phytoplankton concentration in the South China Sea.

Methods The flying speed was around 55 m/s; given that the repetition rate of the laser is 100 Hz, 500 frames of airborne data obtained in 5 s will be accumulated to extend the dynamic range of the detector system. This study will use the Klett method to inverse the airborne data from offshore water to coastal water. The attenuation coefficient of 486 nm and 532 nm channels was retrieved with the Klett method to compare the difference in coefficients between coastal water and oceanic water. The detectors equipped in the DWOL are photomultiplier tube (PMT) detectors. The PMTs will generate a series of after-pulse count (APC) noises after receiving strong returning signals from the upper water, which will mislead the inversion results from the deep water. To avoid the effect of APC and the saturated data returning from the water surface, the airborne data from 80 m to 6 m underwater will be used to analyze the distribution of subsurface chlorophyll concentration. The correction between the shipborne inversed results and the *in-situ* measurement results will be analyzed to validate the effectiveness of the inversed airborne results. Finally, the swath of about 120 km was selected, and the Chl-a concentration based on the airborne data from the selected swath was inversed to analyze the distribution of Chl-a in the South China Sea.

Results and Discussions The profiles of backscattering signals recorded with 486 nm channel and 532 nm channel in continuous 5 s were accumulated to enhance the dynamic range of the detecting system after the effect of after-pulse noise induced by the strong signals from upper water was removed (Fig. 4). The results [Fig. 4(a)] show that the backscattering signals obtained with 486 nm channel are about 25% deeper than those obtained with 532 nm channel, although the attenuation trend in coastal water is almost the same [Fig. 4(b)]. The inversed results of airborne data in coastal water and oceanic water (Fig. 5) show that the attenuation coefficient of 532 nm channel is larger than that of 486 nm channel, which means the 486 nm laser is more suitable for detecting oceanic water. However, the attenuation coefficients of 486 nm and 532 nm channels are virtually equal in coastal water, indicating that the 532 nm laser becomes more suitable for coastal water detection. The asynchronous shipborne experiment was conducted in coastal water and oceanic water. The synchronous shipborne measurement results show that, in oceanic water, the maximum chlorophyll concentration is at 60 m underwater (Fig. 7); the maximum chlorophyll concentration in coastal water ranges from 40 to 20 m underwater (Fig. 6). The correction analysis between the inversed airborne results and the *in-situ* shipborne results shows that the determination coefficient of correlation between the inversed airborne data and the *in-situ* shipborne data is above 0.8 (Fig. 9), indicating that the inversed airborne data and the *in-situ* shipborne measurement results are in good agreement. A flight swath was selected from the tracks, which began the offshore water Swath-A to the coastal water Swath-B and was about 120 km in total. The inversed results of chlorophyll concentration based on the airborne from the selected swath are shown in Fig. 10. The result (Fig.10) shows that the subsurface chlorophyll scattering layer is meanly suspended at 60 m underwater in the offshore water. When the tracks are near coastal water, the subsurface chlorophyll scattering layer raises rapidly and is suspended from 40 to 20 m underwater because the water becomes shallower near the coastal line.

Conclusions In this study, we describe a unique dual-wavelength lidar system that simultaneously uses 532 and 486 nm lasers. An aerial experiment and a synchronized shipborne *in-situ* measurement experiment were undertaken in the South China Sea to test the performance of the dual-wavelength lidar. The inversed findings of attenuation coefficients for the 486 nm and 532 nm channels reveal that the 486 nm blue laser is better for detecting oceanic water, whereas the 532 nm green laser is better for detecting coastal water. The continuous inversed results of Chl-a concentration from coastal water to oceanic water show that the subsurface chlorophyll scattering layer in the oceanic water is primarily suspended at 60 m underwater. In contrast, the chlorophyll scattering layer in coastal water is mainly suspended between 40 m to 20 m underwater. The determination coefficient of correlation between the inversed aerial results and the *in-situ* shipborne measurement results is more significant than 0.8, showing compelling inversed airborne results.

Key words remote sensing; dual-wavelength lidar; chlorophyll scattering layer; lidar inversion; Klett method

OCIS codes 010.3640; 010.4450; 120.0280